The boundary element method for light scattering by ice crystals and its implementation in BEM++

S. P. Groth[a,*], A. J. Baran[b], T. Betcke[c], S. Havemann[b], W. Śmigaj[d]

[a]*Department of Mathematics and Statistics, University of Reading, Whiteknights PO Box 220, Reading, RG6 6AX, UK*
[b]*Met Office, Fitzroy Road, Exeter, Devon EX1 3PB, UK*
[c]*Department of Mathematics, University College London, Gower Street, London, WC1E 6BT, UK*
[d]*Simpleware, Bradninch Hall, Castle Street, Exeter, EX4 3PL, UK*

Abstract

A number of methods exist for solving the problem of electromagnetic scattering by atmospheric ice crystals. Amongst these methods, only a few are used to generate "benchmark" results in the atmospheric science community. Most notably, the T-matrix method, Discrete Dipole Approximation, and the Finite-Difference Time-Domain method. The Boundary Element Method (BEM), however, has received considerably less attention in this community despite its extensive use and development in other areas of applied mathematics and engineering. Recently the group of Betcke et. al. [4] at University College London has released a high performance open source boundary element library called BEM++. In this paper, we employ BEM++ to calculate the scattering properties of hexagonal ice columns of fixed orientation, as well as more complicated particles such as hollow columns and bullet-rosettes. The results for hexagonal columns are compared to those obtained using a highly accurate and well-established T-matrix method [3] for a range of different wavelengths and size parameters. It is shown that the results are in excellent agreement and that BEM++ is a fast alternative to the T-matrix method and others for generating benchmark results. However, the large memory requirements of BEM++ cause it to be limited to size parameters ~15 on a standard desktop PC if an accuracy of roughly 1% is required. The main advantages of BEM++ over many other methods are its flexibility to be applied to homogeneous dielectric particles of arbitrarily complex shape, and its open availability. This flexibility is illustrated by the application of BEM++ to scattering by hollow columns with different cavity types, as well as bullet-rosettes with 2 to 6 branches.

Keywords: Electromagnetic scattering, boundary element method, cirrus

1. Introduction

It has been well established that understanding the scattering properties of atmospheric ice crystals is important in modelling the radiation balance of cirrus clouds [1, 2, 17]. Due to the wide coverage of cirrus over the Earth (~30% at any one time in the mid-latitudes, and ~60-80% in the tropics [1, 17, 26]), these clouds in turn play an important role in the earth-atmosphere radiation balance.

The ice crystals within cirrus exhibit a large array of sizes and shapes [14, 10, 16]. This, combined with the frequency range of radiation incident upon the clouds (from microwave to ultraviolet), leads to a huge variety of scattering problems to be solved. Over the years, many methods have been developed for tackling different problems within the myriad combinations of particle shape, size and incident radiation frequency. These methods fall into two main camps.

The first contains asymptotic or "approximate" methods which utilise the high-frequency behaviour of light to justify the implementation of geometrical techniques. Examples include Geometric Optics [18], the Kirchhoff approximation [23, 32, 5], and Ray Tracing with Diffraction on Facets [13]. These methods are applicable to particles of large size parameter.

The second camp contains so-called "exact" methods which either discretise the underlying Maxwell's equations and solve the resultant discrete system, or propose a separation of variables ansatz and obtain the

---

*Corresponding author
Email address: s.groth@pgr.reading.ac.uk (S. P. Groth)

coefficients by enforcing the boundary conditions at the ice crystal's surface. Such methods include the T-matrix method [12, 22, 15], the invariant imbedding T-matrix method [6], the Discrete Dipole Approximation (DDA) [34], and Finite-Difference Time-Domain method (FDTD) [29]. These methods have a computational cost that scales with size parameter and hence are typically feasible only at small to moderate size parameters. We note briefly that exact methods which bridge these two camps exist. However their development is still in its early stages and, at present, they are limited to scalar problems (see e.g. [9, 11]).

One "exact" method that has received scant attention in the atmospheric physics community, apart from some application to simple shapes with exploitable symmetries [19, 24], is the Boundary Element Method (BEM) which, in it most standard form (i.e., not hybrid, see [9]), is applicable to small to moderate size parameter particles of arbitrary shape and at any wavelength. Moreover, a high-performance boundary element library called BEM++ has recently been developed and made open-source at `http://www.bempp.org` by the group of Betcke et. al. [27].

Within the BEM framework, Maxwell's equations are reformulated as a system of boundary integral equations on the particle's surface via the Stratton-Chu formulae. This has the advantage of reducing a problem defined on a three-dimensional infinte domain to a problem defined on a two-dimensional finite domain. The equations are solved to obtain the electric and magnetic surface currents which may then be substituted into the Stratton-Chu formulae (or their far-field asymptotic form) to obtain the field anywhere.

This paper analyses the performance of BEM++ in its application to the scattering problems associated with atmospheric non-spherical ice. In particular, its performance is compared to that of a well-established standard T-matrix method [12] for the problem of scattering by hexagonal ice columns. We go on to demonstrate BEM++'s utility for scattering problems involving complex particle shapes, such as hexagonal columns with cavities and bullet-rosettes. The single-scattering properties we consider in this paper are not at present direct outputs from BEM++. However, example Python scripts which generate these from BEM++'s output can be downloaded from the corresponding author's webpage `http://www.personal.reading.ac.uk/~xk023928/`.

The paper is organised as follows. In section 2, we state the electromagnetic scattering problem to be solved. Section 3 gives a brief outline of the reformulation of the problem as a system of boundary integral equations, which is performed utilising the Stratton-Chu formulae. Section 4 recalls the definitions of the amplitude scattering matrix and other important scattering properties, and also how they are computed from the outputs of BEM++. In section 5, the settings of various error tolerances within BEM++ are discussed. Sections 6,7 and 8 comprise the results portion of the paper. Section 6 compares the solution of scattering by a sphere with BEM++ to the exact solution, obtained via Mie-Lorenz theory, in order to ascertain the accuracy of BEM++ and decide upon the appropriate mesh resolution to be used. Section 7 looks at scattering by hexagonal columns, comparing the solution with BEM++ to that obtained using a T-matrix method. In section 8 BEM++ is applied to scattering by hexagonal columns with different types of cavity, and bullet-rosettes, problems which are beyond the applicability of current standard T-matrix methods. The final section contains some discussion and concluding remarks.

2. Problem statement

Consider the scattering of a monochromatic plane wave with time-dependence $e^{-i\omega t}$ by a homogeneous, isotropic dielectric scatterer Ω_1 (see Figure 1) with a complex refractive index $n = \sqrt{\epsilon\mu}$, where ϵ and μ are the permittivity and permeability, respectively, of the material composing Ω_1. It is assumed that Ω_1 is surrounded by a homogeneous medium $\Omega_2 := \mathbb{R}^3 \backslash \overline{\Omega_1}$ with unit refractive index.
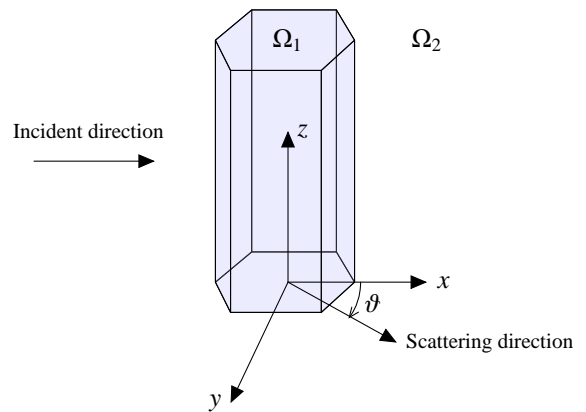

Figure 1: Scattering setup

The transmission problem is to find the fields $\{\mathbf{E}_1, \mathbf{H}_1\}$ and $\{\mathbf{E}_2, \mathbf{H}_2\}$ in Ω_1 and Ω_2 respectively, satisfying

Maxwell's equations

$$\nabla \times \mathbf{E_1} = i\omega\mu_1\mathbf{H}_1, \quad \nabla \times \mathbf{H}_1 = -i\omega\epsilon_1\mathbf{E}_1 \quad \text{in } \Omega_1, \quad (1)$$

$$\nabla \times \mathbf{E_2} = i\omega\mu_2\mathbf{H}_2, \quad \nabla \times \mathbf{H}_2 = -i\omega\epsilon_2\mathbf{E}_2 \quad \text{in } \Omega_2, \quad (2)$$

along with the *transmission conditions* on the interface $\Gamma := \partial\Omega_1$:

$$\mathbf{n} \times \mathbf{E}_1 = \mathbf{n} \times \mathbf{E}_2 \quad \text{and} \quad \mathbf{n} \times \mathbf{H}_1 = \mathbf{n} \times \mathbf{H}_1. \quad (3)$$

In addition, the scattered fields, defined as $\mathbf{E}^s := \mathbf{E}_2 - \mathbf{E}^i$, $\mathbf{H}^s := \mathbf{H}_2 - \mathbf{H}^i$ where $\{\mathbf{E}^i, \mathbf{H}^i\}$ is the incident electromagnetic field, are required to satisfy the Silver-Müller radiation condition

$$\sqrt{\mu}\hat{\mathbf{x}} \times \mathbf{H}^s + \sqrt{\varepsilon}\mathbf{E^s} = o\left(\frac{1}{r}\right) \quad \text{as} \quad r := |\mathbf{x}| \to \infty \quad (4)$$

uniformly in all directions $\hat{\mathbf{x}} := \mathbf{x}/r$.

In this paper, we are considering scattering by ice crystals in air for which $\mu_1 = \mu_2 = 1$. Also, all examples considered here are for particles in fixed orientation with the incident wave travelling in the positive x-direction, as shown in Figure 1.

3. Boundary Integral Equations

We briefly summarise the reformulation of the transmission problem as a system of boundary integral equations. The exposition here follows that of [27] which in turn closely follows [8]; the latter gives an in-depth review of the the boundary integral formulation for this problem.

It is sufficient to solve for one of the two fields $\mathbf{E}$ and $\mathbf{H}$ due to their relationship in Maxwell's equations (1-2). Here we choose the electric field $\mathbf{E}$, for which the transmission conditions on Γ may be written as

$$\mathbf{n} \times \mathbf{E}_1 = \mathbf{n} \times \mathbf{E}_2, \quad \mathbf{n} \times (\nabla \times \mathbf{E}_1) = \frac{\mu_1}{\mu_2}\mathbf{n} \times (\nabla \times \mathbf{E}_2). \quad (5)$$

We begin by defining the trace operators necessary for restricting our attention to the boundary of the scatterer. The Dirichlet trace is defined as

$$\gamma_D\mathbf{E}(\mathbf{x}) := \mathbf{n}(\mathbf{x}) \times \mathbf{E}(\mathbf{x})|_\Gamma,$$

where $\mathbf{n}$ is the outward normal to Γ. The Neumann trace is defined as

$$\gamma_N\mathbf{E}(\mathbf{x}) := \frac{1}{ik}\mathbf{n}(\mathbf{x}) \times (\nabla \times (\mathbf{E}(\mathbf{x}))|_\Gamma.$$

Note that here (for the Neumann trace) we are following [27]. This differs from the definition in [8] in that it

includes an extra i factor in the denominator. The traces from the exterior and interior shall be written γ_D^+, γ_N^+ and γ_D^-, γ_D^-, respectively. Now the transmission conditions (5) can be stated in the concise way:

$$\gamma_D^+\mathbf{E}_1 = \gamma_D^-\mathbf{E}_2 \quad \text{and} \quad \frac{k_1}{\mu_1}\gamma_N^+\mathbf{E}_1 = \frac{k_2}{\mu_2}\gamma_N^-\mathbf{E}_2 \quad \text{on } \Gamma. \quad (6)$$

In order to state the Stratton-Chu formulae, as well as the following formulae, it is useful to define the single-layer potential operator Ψ_{SL} and double-layer potential operator Ψ_{DL}:

$$\Psi_{SL}v(\mathbf{x}) := ik \int_\Gamma G_k(\mathbf{x}, \mathbf{y})v(\mathbf{y})d\Gamma(\mathbf{y})$$
$$- \frac{1}{ik}\nabla \int_\Gamma G_k(\mathbf{x}, \mathbf{y})\nabla \cdot v(\mathbf{y})d\Gamma(\mathbf{y})$$

and

$$\Psi_{DL}v(\mathbf{x}) := \nabla \times \int_\Gamma G_k(\mathbf{x}, \mathbf{y})v(\mathbf{y})d\Gamma(\mathbf{y}),$$

where G_k is the Green's function of the Helmholtz equation with wavenumber k:

$$G_k(\mathbf{x}, \mathbf{y}) = \frac{\exp(ik|\mathbf{x} - \mathbf{y}|)}{4\pi|\mathbf{x} - \mathbf{y}|}.$$

Now an integral representation for $\mathbf{E}$ in Ω_1 can be written succinctly as

$$\mathbf{E}(\mathbf{x}) = \Psi_{DL}\gamma_D^+\mathbf{E}(\mathbf{x}) + \Psi_{SL}\gamma_N^-\mathbf{E}(\mathbf{x}), \quad \mathbf{x} \in \Omega_1. \quad (7)$$

Similarly, $\mathbf{E}$ in Ω_2 possesses the representation

$$\mathbf{E}(\mathbf{x}) = -\Psi_{DL}\gamma_D^+\mathbf{E}(\mathbf{x}) - \Psi_{SL}\gamma_N^+\mathbf{E}(\mathbf{x}), \quad \mathbf{x} \in \Omega_2. \quad (8)$$

These are the Stratton-Chu representation formulae and are often written in a more explicit form without potential operators. For these expressions the reader is referred to [20] and [25].

Boundary integral operators are constructed by applying the Dirichlet and Neumann traces $\gamma_D^\pm, \gamma_N^\pm$ to the potentials Ψ_{SL} and Ψ_{DL}. We might expect to obtain four different boundary integral operators, however due to the fact that $\nabla \times \Psi_{SL} = k\Psi_{DL}$ and $\nabla \times \Psi_{DL} = k\Psi_{SL}$, we have that

$$\gamma_N^\pm\Psi_{SL} = \gamma_d^\pm\Psi_{DL}, \quad \gamma_N^\pm\Psi_{DL} = \gamma_D^\pm\Psi_{SL}.$$

Hence two different boundary integral operators are sufficient for electromagnetic scattering. We define them as

$$\mathcal{S}_k := \gamma_D\Psi_{SL} = \gamma_N\Psi_{DL}, \quad \mathcal{C}_k := \gamma_D\Psi_{DL} = \gamma_N\Psi_{SL}.$$

3

Applying the interior and exterior traces to the Stratton-Chu formulae, we arrive at the boundary integral equations [8]

$$\left(-\frac{1}{2}I + C_-\right)\gamma_D^- \mathbf{E} + S_-\gamma_N^- \mathbf{E} = 0 \tag{9}$$

$$-S_i\gamma_D^- \mathbf{E} + \left(-\frac{1}{2}I + C_-\right)\gamma_N^- \mathbf{E} = 0 \tag{10}$$

$$\left(\frac{1}{2}I + C_+\right)\gamma_D^+ \mathbf{E} + S_+\gamma_N^+ \mathbf{E} = \gamma_D^+ \mathbf{E}^i \tag{11}$$

$$-S_+\gamma_D^+ \mathbf{E} + \left(\frac{1}{2}I + C_+\right)\gamma_N^+ \mathbf{E} = \gamma_N^+ \mathbf{E}^i. \tag{12}$$

Writing (9) and (10) in terms of exterior traces by using the transmission conditions $\gamma_D^+ u = \gamma_D^- u$, $\frac{k_2}{\mu_2}\gamma_N^+ u = \frac{k_1}{\mu_1}\gamma_N^- u$, and writing $\rho = \frac{\mu_2 k_1}{\mu_1 k_2}$:

$$\left(-\frac{1}{2}I + C_-\right)\gamma_D^+ \mathbf{E} + \frac{1}{\rho}S_-\gamma_N^+ \mathbf{E} = 0 \tag{13}$$

$$-S_-\gamma_D^+ \mathbf{E} + \frac{1}{\rho}\left(-\frac{1}{2}I + C_-\right)\gamma_N^+ \mathbf{E} = 0. \tag{14}$$

We have arrived at four boundary integral equations for the two unknowns $\gamma_D \mathbf{E}$ and $\gamma_N \mathbf{E}$. There are numerous ways to select two equations or two linear combinations of (13), (14), (11) and (12); see [20] for a discussion of five of these. Here we choose the simplest, the *combined-field formulation*, which is known to be uniquely solvable [21]. This consists of taking the two combinations

$$(11) + (13) \quad \text{and} \quad (12) + (14).$$

After dropping the $\pm$ on the traces, we have the system of boundary integral equations to be solved:

$$\begin{pmatrix} C_+ + C_- & S_+ + \frac{1}{\rho}S_- \\ -S_+ - \rho S_- & C_+ + C_- \end{pmatrix}\begin{pmatrix} \gamma_D \mathbf{E} \\ \gamma_N \mathbf{E} \end{pmatrix} = \begin{pmatrix} \gamma_D \mathbf{E}^i \\ \gamma_N \mathbf{E}^i \end{pmatrix}. \tag{15}$$

Once this system is solved for $\mathbf{E}$ and its normal derivative on Γ, the solution is simply substituted into (7) or (8) to obtain the solution anywhere in $\mathbb{R}^3$. If it is the far-field solution which is of interest, we must use the asymptotic (large kr) form of (8). This is discussed in the following section.

4. Single scattering properties and problem setup

4.1. Amplitude scattering matrix

In the application of interest in this paper, it is the scattered far-field which is of most importance. This is due to the fact that ice crystals in cirrus tend to be separated by large enough distances such that $kr >> 1$, hence they are in each other's far-fields. The scattered far-field is obtained using the asymptotic form of equation (8), i.e.

$$\mathbf{E}^s(\mathbf{x}) \sim -\frac{e^{ikr}}{r}\mathbf{F}(\mathbf{x}), \quad \text{as } kr \to \infty, \tag{16}$$

where

$$\mathbf{F}(\mathbf{x}) = \Psi_{DL}^F(\gamma_D^+ \mathbf{E}) + \Psi_{SL}^F(\gamma_N^+ \mathbf{E}).$$

Here we are using the far-field versions of the single- and double-layer potentials, defined as

$$[\Psi_{DL}^F v](x) = \frac{-ik}{4\pi}\int_\Gamma e^{-ik(\mathbf{x}\cdot\mathbf{y})/|\mathbf{x}|}\left(\frac{\mathbf{x}}{|\mathbf{x}|}\times v(\mathbf{y})\right)d\Gamma((y)) \tag{17}$$

$$[\Psi_{SL}^F v](x) = -\frac{ik}{4\pi}\int_\Gamma e^{-ik(\mathbf{x}\cdot\mathbf{y})/|\mathbf{x}|}v(\mathbf{y})d\Gamma(\mathbf{y})$$
$$+ \frac{ik}{4\pi}\int_\Gamma e^{-ik(\mathbf{x}\cdot\mathbf{y})/|\mathbf{x}|}v(\mathbf{y})\cdot\frac{\mathbf{x}}{|\mathbf{x}|}d\Gamma(\mathbf{y}). \tag{18}$$

These far-field potentials are functions in BEM++ and so the far-field pattern is easily calculated. Equation (16) encapsulates the standard far-field definition in the boundary integral equation literature. However, it must be noted that it differs from the definition in physics texts (such as [7]), where we find it written

$$\mathbf{E}^s(\mathbf{x}) \sim -\frac{e^{ikr}}{ikr}\tilde{\mathbf{F}}(\mathbf{x}).$$

In order to account for this difference, the far-field output of BEM++ must be multiplied by ik since

$$\tilde{\mathbf{F}}(\mathbf{x}) = ik\mathbf{F}(\mathbf{x}).$$

The output of the above far-field calculation in (16) in BEM++ is of the scattered field in Cartesian coordinates (x, y, z) in a given scattering direction $\hat{\mathbf{e}}^r$, as shown in Figure 1. It is useful to define the direction $\hat{\mathbf{e}}^r$ in terms of the angles ϑ and ϕ. ϕ dictates the scattering plane and is a rotation about the y-axis, and ϑ describes the scattering direction within that scattering plane. Explicitly, the direction vector is written

$$\hat{\mathbf{e}}^r = (\cos(\vartheta), \cos(\phi)\sin(\vartheta), \sin(\phi)\cos(\vartheta)). \tag{19}$$

When calculating the scattering matrix entries, we shall focus on the plane $\phi = 0$, hence

$$\hat{\mathbf{e}}^r = (\cos(\vartheta), \sin(\vartheta), 0)$$

for $0 < \vartheta < 2\pi$.

4

We note that the scattered far-field is transverse, $\hat{\mathbf{e}}^r \cdot \tilde{\mathbf{F}} = 0$, hence it may be written

$$\mathbf{E}^s = (E_\parallel^s \hat{\mathbf{e}}_{\parallel s} + E_\perp^s \hat{\mathbf{e}}_{\perp s})e^{ikr},$$

where (in the case $\phi = 0$)

$$\hat{\mathbf{e}}_{\parallel s} = \hat{\mathbf{e}}_\vartheta, \quad \hat{\mathbf{e}}_{\perp s} = \hat{\mathbf{z}}, \quad \hat{\mathbf{e}}_{\perp s} \times \hat{\mathbf{e}}_{\parallel s} = \hat{\mathbf{e}}_r,$$

following the notation of [7]. The BEM++ output far-field can be converted to this new form simply by the transformation

$$E_{\parallel s}^s = -\sin(\vartheta)E_x^s + \cos(\vartheta)E_y^s, \quad E_{\perp s}^s = E_z^s. \quad (20)$$

In a similar way, the incident field is written in terms of its frame as

$$\mathbf{E}^i = (E_{\parallel i}^i \hat{\mathbf{e}}_{\parallel i} + E_{\perp i}^i \hat{\mathbf{e}}_{\perp i})e^{ikx},$$

where, in this case,

$$\hat{\mathbf{e}}_{\parallel i} = \hat{\mathbf{y}} \quad \text{and} \quad \hat{\mathbf{e}}_{\perp i} = \hat{\mathbf{z}}.$$

The *Amplitude Scattering Matrix* defines the relationship between the scattered far-field and the *arbitrarily polarised* incident field in their respective coordinate frames, i.e.

$$\begin{pmatrix} E_{\parallel s}^s \\ E_{\perp s}^s \end{pmatrix} = \frac{e^{ik(r-x)}}{-ikr} \begin{pmatrix} A_{11} & A_{12} \\ A_{21} & A_{22} \end{pmatrix} \begin{pmatrix} E_{\parallel i}^i \\ E_{\perp i}^i \end{pmatrix} \quad (21)$$

In order to calculate all entries A_{ij}, we consider two separate incident waves with different polarisations: one polarised in the $\hat{\mathbf{z}}$-direction and the other polarised in the $\hat{\mathbf{y}}$-direction. Each wave has unit amplitude and travels in the positive x-direction, as depicted in Figure 1. Let us consider these two problems separately.

4.1.1. $\hat{\mathbf{z}}$-polarised incident wave

In this case the incident wave has the form

$$\mathbf{E}^i = (1 \cdot \hat{\mathbf{e}}_{\perp i} + 0 \cdot \hat{\mathbf{e}}_{\parallel i})e^{ikx}$$

and thus it is possible to calculate two of the matrix entries, namely A_{12} and A_{22}. They are given as

$$A_{12} = -\sin(\vartheta)E_x^s + \cos(\vartheta)E_y^s, \quad A_{22} = E_z^s. \quad (22)$$

4.1.2. $\hat{\mathbf{y}}$-polarized incident wave

In this case the incident wave has the form

$$\mathbf{E}^i = (1 \cdot \hat{\mathbf{e}}_{\parallel i} + 0 \cdot \hat{\mathbf{e}}_{\perp i})e^{ikx}$$

and thus it is possible to calculate two of the matrix entries, namely A_{11} and A_{21}. They are given as

$$A_{11} = -\sin(\vartheta)E_x^s + \cos(\vartheta)E_y^s, \quad A_{21} = E_z^s. \quad (23)$$

4.2. *Scattering phase function; scattering, extinction and absorption cross sections; and asymmetry parameter*

Now that the amplitude scattering matrix has been obtained, one may proceed to calculate the entries of the so-called *scattering matrix* as in, e.g., [7]. Its first entry is given as

$$S_{11} = \frac{1}{2}(|A_{11}|^2 + |A_{22}|^2 + |A_{21}|^2 + |A_{12}|^2). \quad (24)$$

This entry is often normalised in the following manner

$$P_{11} = \frac{4\pi S_{11}}{k^2 C_{sca}}$$

and referred to as the *dimensionless phase function* and denoted $\mathcal{P}(\vartheta)$. Here C_{sca} is the scattering cross section defined as

$$C_{sca} = \int_0^{2\pi} \int_0^\pi \frac{S_{11}}{k^2} \sin\vartheta d\vartheta d\phi, \quad (25)$$

that is, the scattering cross section is the integral of the far-field amplitude over all scattering directions $\hat{\mathbf{e}}_r$. The extinction cross section is defined as

$$C_{ext} = \frac{4\pi}{k^2} Re\left\{(S_{11} \cdot \hat{\mathbf{e}})_{\vartheta=0}\right\}. \quad (26)$$

The absorption cross section is defined as the difference of the two:

$$C_{abs} = C_{ext} - C_{sca}. \quad (27)$$

The quantities that shall be discussed later are the normalised version of these parameters. More precisely they are the scattering, extinction and absorption efficiencies defined as

$$Q_{sca} = \frac{C_{sca}}{P}, \quad Q_{ext} = \frac{C_{ext}}{P}, \quad Q_{abs} = \frac{C_{abs}}{P},$$

where P is the geometric cross section of the particle projected onto a plane perpendicular to the incident wave direction. Another useful quantity for which we present calculated values is the *single-scattering albedo*, defined as

$$\omega_0 = \frac{Q_{sca}}{Q_{ext}}.$$

Finally, the *asymmetry parameter* is defined as

$$g = \int_{4\pi} p\cos\vartheta d\Omega = \int_0^{2\pi} \int_0^\pi p\cos\vartheta \sin\vartheta d\vartheta d\phi,$$

$$= \frac{1}{k^2 C_{sca}} \int_0^{2\pi} \int_0^\pi S_{11}\cos\vartheta \sin\vartheta d\vartheta d\phi, \quad (28)$$

5

where p is the *phase function* $p = \mathcal{P}/4\pi$.

These quantities are, at present, not direct outputs of BEM++. However, as illustrated above, can be generated from BEM++ far-field calcuations. In what follows, we shall compare the calcuations of these scattering properties in BEM++ to those obtained using Mie-Lorenz theory in the case of scattering by spheres, and using the T-matrix method of [12] in the case of hexagonal columns. We shall go on to calculate these scattering properties with BEM++ alone for more complex particles for which this current T-matrix code is not applicable.

5. Solution with BEM++

Currently BEM++ provides a single discrete approximation space for approximating $\gamma_D u$ and $\gamma_N u$, namely the space of lowest-order Raviart-Thomas functions. This leaves mesh refinement as the only way to increase the accuracy of the approximation. In the next section, we illustrate how the accuracy of BEM++, in approximating scattering by a dielectric sphere, varies with mesh refinement. That is, we vary the number of mesh elements per wavelength. It is found that the standard engineering rule of thumb of "10 elements per wavelength" is sufficient to achieve approximately 1% accuracy. Higher resolution meshes generate more accurate approximations (as we shall we in §6) however at the cost of increased CPU time and memory requirements.

There are various tolerances to be set in BEM++ for the different algorithms it employs. These tolerance values were chosen after experiementation and led by examples provided on the BEM++ webpage, along with [4]. It was found that these values are sufficient to cause the accuracy of the solution to be dominated by the mesh size. We state the tolerances, although they can be found in the example Python scripts provided on the corresponding author's webpage. The adaptive cross approximation (ACA) tolerance is set as $1e-5$, and the generalised minimal residual (GMRES) tolerance as $1e-8$. The accuracy of the LU decomposition is chosen as $1e-2$. Finally, the accuracy of the single and double regular integral quadrature was increased by 2.

It should be noted that there are other ACA settings such as the maximum rank and maximum block size that may be altered to improve the performance of BEM++. It was found here, however, that for the relatively small scale computations performed in this paper, altering these settings from their defaults made a negligible difference. For large scale computations, it is expected that adjusting these ACA settings will affect the performance of BEM++, with the optimal settings being dependent on the specifications of the computer/s being used.

6. Scattering by spheres - comparison with Mie-Lorenz theory

To get a measure of the speed, accuracy and convergence rate of BEM++, we first examine the case of scattering by an ice sphere with $ka = 5$ and refractive index $n = 1.0893 + 0.18216i$, where a is the radius of the sphere. The complex refractive indices used in this paper are taken from the study in [31].

In the following numerical experiments, we consider meshes of increasing refinement, starting from an element size of $h = \lambda/2.5$ and doubling the refinement for each successive numerical experiment until we reach an element size of $h = \lambda/40$. For each level of refinement, we record the memory requirement for the operator $\mathcal{S}_-$, the total run time, along with the errors of the asymmetry parameter and the scattering and extinction efficiencies. The errors given are relative, e.g. $|Q_{sca}(BEM) - Q_{sca}(Mie)|/Q_{sca}(Mie)$. Table 1 displays this information. It can be seen from the table that the

h	Mem. (MB)	Time (s)	Q_{sca} err.(%)	Q_{ext} err.(%)	g err.(%)
$\lambda/2.5$	1.73	2.15	1.27e1	1.12e1	1.23e0
$\lambda/5$	10.6	9.07	5.41e0	4.38e0	2.55e-1
$\lambda/10$	53.6	37.0	1.87e0	1.34e0	4.93e-2
$\lambda/20$	313	199	5.33e-1	2.99e-1	8.14e-3
$\lambda/40$	1500	933	2.59e-1	8.81e-2	3.50e-3

Table 1: Scattering by a sphere with $ka = 5$ and $n = 1.0893 + 0.18216i$. Memory use for operator $\mathcal{S}_-$, run time, and relative error (%) in the approximation of Q_{sca}, Q_{ext} and g at each mesh refinement.

memory cost of BEM++ increases by approximately a factor 5 each time the refinement of the mesh is doubled. We observe that the BEM is around 1-2% accurate at a mesh size of $h = \lambda/10$ when approximating Q_{sca} and Q_{ext}, but 0.05% accurate when approximating g at this resolution. Hence it appears that if g is the only parameter of interest, such a fine mesh is not necessary. In fact, with 2.5 elements per wavelength, we achieve ~1% accuracy in g.

Figure 2 shows the scattering phase function calculated using Mie-Lorenz theory and BEM++ at two different resolutions: $\lambda/2.5$ and $\lambda/10$. It is evident that at the $\lambda/10$ resolution, BEM++ approximates the phase
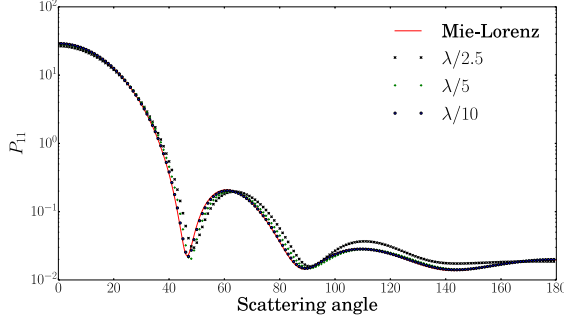
Figure 2: Phase function for a sphere with size parameter $ka = 5$ and refractive index $n = 1.0893 + 0.18216i$. Convergence of P_{11} to exact Mie solution as the mesh is refined.

function extremely well. In fact, the relative L^2 error of the approximation of the phase function here is 0.69%.

Figure 3 shows P_{11} for a sphere with size parameter $ka = 15$ and refractive index $n = 1.311 + 2.289e - 9i$. There is no discernible difference in the phase function,
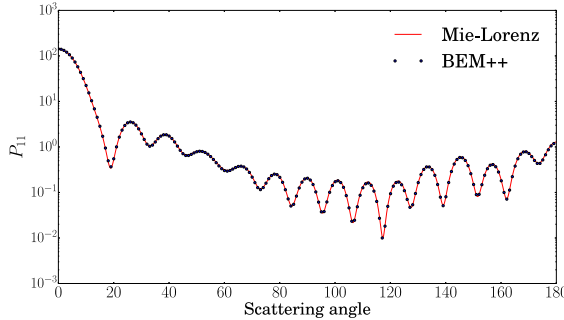

Figure 3: Phase function for a sphere with size parameter $ka = 15$ and refractive index $n = 1.311 + 2.289e - 9i$ calculated with Mie-Lorenz theory and BEM++ at a resolution of $\lambda/10$.

in fact, its error in the L^2 norm is 0.4%. The errors in C_{sca} and C_{ext} are again between 1% and 2%. In the next section, we examine the capabilities of BEM++ when applied to a commonly occuring ice crystal shape in cirrus - the hexagonal column.

7. Scattering by hexagonal ice columns - comparison with T-matrix

In this section, we compare the performance of BEM++ to that of the T-matrix method of [12] for scattering by hexagonal ice columns. In the previous sec-

tion it was established that a mesh resolution of $\lambda/10$ is sufficient to produce approximately 1% accuracy with BEM++. The simulations run in this section shall be at this resolution. Comparisons are made for hexagonal ice columns with refractive index $n = 1.311 + 2.289e - 9i$ of three size parameters ($ka = 5, 10, 15$). The incident wave direction and orientation of the hexagonal ice column are both as illustrated in Figure 1.

The aspect ratio of the hexagonal column is the ratio L/a where L is the height of the column and a is the radius of the smallest circle which enscribes the hexagonal face. Throughout we take this ratio to be 2. We note that we maintain the definition of size parameter as ka, whereas some authors use the definition kL which would lead to a doubling of all the size parameter figures given here for the hexagonal ice columns.

Table 2 displays some of the performance details for the two methods. BEM++, which has been optimised for computations in parallel, was run on 4 core machine with a total of 16.4 Gigabytes of RAM, whereas the T-matrix code was run on a single core of the same machine. The memory requirements for BEM++ shown

ka	CPU (s) (T)	CPU (s) (BEM)	Mem. (MB) (T)	Mem. (MB) (BEM)
5	319	65.5	3.81	496
10	7470	471	34.3	2420
15	27600	1720	92.3	7050

Table 2: CPU time and memory load utilised (given to 3 significant figures) by the T-matrix and BEM++ to calculate the scattering properties of hexagonal ice columns of different size parameters.

in the table are those required to store the four operators $\mathcal{S}_+, \mathcal{S}_-, \mathcal{C}_+, \mathcal{C}_-$ that compose the system matrix in (15). Simiarly, the memory requirement figures shown for the T-matrix relate to the memory required to store the system matrix arising in that method. It is evident from the table that the memory utilised by the BEM is currently much greater than that utilised by the T-matrix code. This memory consumption is the main drawback of most BEMs (with the exception of some 2D high frequency BEMs, see [9]) and is the reason why BEM++ is limited to relatively small size parameters. However, we notice that due to its parallelisation and high-level implementation, BEM++ is extremely fast, with a CPU time more than 16 times faster than the T-matrix for $ka = 15$.

Figure 4 displays phase matrix elements for $ka = 10$. It is clear from the figure that both methods are in excellent agreement. We have omitted P_{22} since it has a
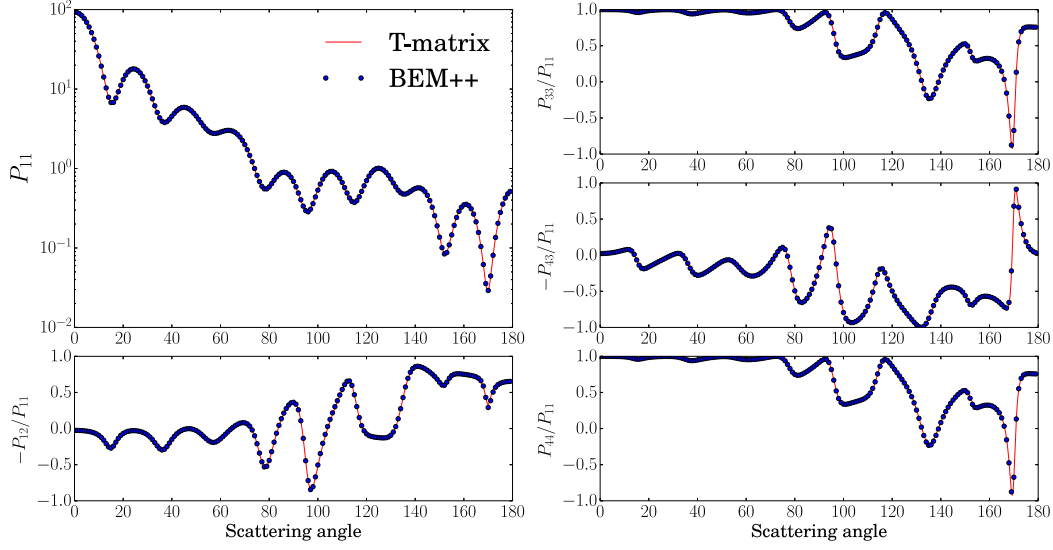
Figure 4: Phase matrix elements as calculated by the T-matrix and BEM++ for $ka = 10$ and $n = 1.311 + 2.289e - 9i$.

value very close to 1 for all scattering angles.

We display the approximations to the scattering and extinction efficiencies, and asymmetry parameter in Table 3. We observe a difference of approximately 2% or less between the two methods at all the size parameters considered.

ka	Q_{sca} (T)	Q_{sca} (BEM)	Q_{ext} (T)	Q_{ext} (BEM)	g (T)	g (BEM)
5	3.74	3.69	3.74	3.72	0.87	0.87
10	2.98	2.92	2.98	2.95	0.78	0.77
15	2.54	2.50	2.54	2.52	0.74	0.74

Table 3: Q_{sca}, Q_{ext} and g calculated using T-matrix and BEM++ for $n = 1.311 + 2.289e - 9i$.

8. Scattering by complex ice crystal shapes using BEM++

In this section we demonstrate the utility of BEM++ for scattering by ice crystal shapes which are beyond the scope of standard T-matrix approaches (although within the scope of the invariant imbedding T-matrix method of [6], the code of which, however, is not as yet in the public domain). Such shapes include bullet-rosettes, aggregates and hexagonal ice columns with cavities. Here we shall focus on hexagonal ice columns with cavities and bullet-rosettes with 1 to 6 branches.

8.1. Hexagonal columns with cavities

We first perform an investigation into the impact of assuming different cavity constructions on the scattering matrix elements. The scattering characteristics are compared for a solid hexagonal column similar to that in §7 to those of columns with both stepped cavities [28] and the more regular pyramidal inclusions [18]. The three shapes are shown in Figure 5. We shall consider two re-
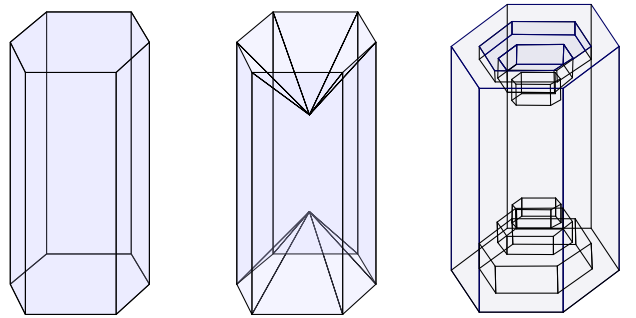

Figure 5: Hexagonal columns: without cavity, with conventional cavity, with stepped cavity.

fractive indices: $1.0833 + 2.04e - 1i$ ($\lambda = 10.87\mu m$) and $1.311 + 2.289e - 9i$ ($\lambda = 0.55\mu m$) in order to observe the effect absorption has upon the differentiation of these particles by their scattering properties. The shape of the
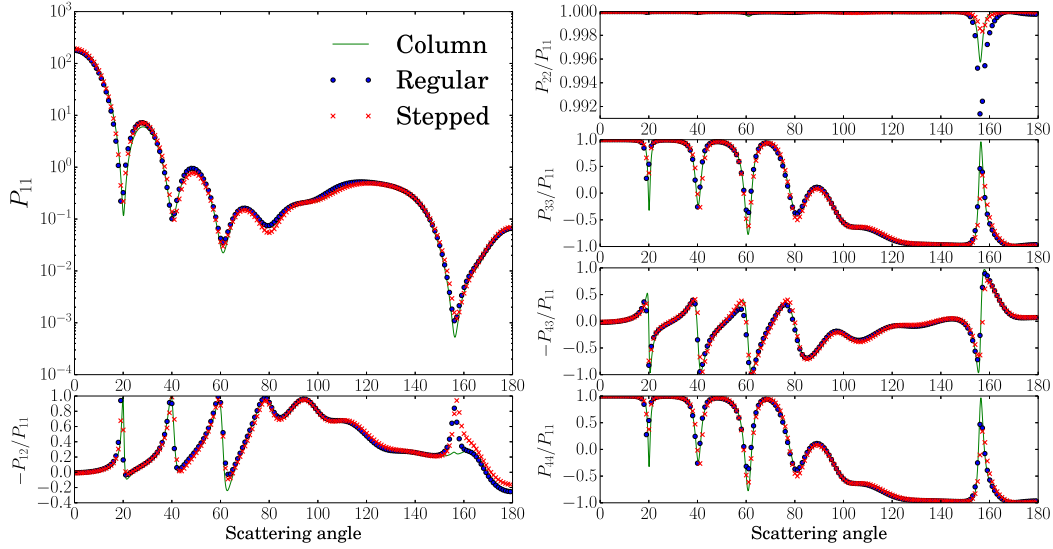
Figure 6: Scattering matrix elements for $n = 1.0833 + 2.04e - 1i$ and $ka = 10$ for the three scatterers in Figure 5.

column with a standard cavity is the same as in [33]. That is, the aspect ratio is $L/a = 1/0.35 \approx 2.857$, and the depth of the cavity is $d = L/4$. The stepped cavity contains three steps, each of depth $d/3$. The radius of the hexagonal faces as we progress down the steps is $a_1 = 0.5a, a_2 = 0.35a, a_3 = 0.2a$. The mesh resolution for these experiments is set at $\lambda/10$, also the incident wave direction and orientation of the columns are both as illustrated in Figure 1.

Figure 6 shows the phase matrix elements for the three shapes at $ka = 10$ and for $n = 1.0833 + 2.04e - 1i$. It is clear that at this highly absorbing wavelength, the phase matrix is almost idential for all 3 shapes. One exception is at the scattering angle of 156°. Here we observe the scattering pattern from the hollow columns differs slightly from that of the solid column.

Table 4 shows the scattering efficiencies and the asymmetry parameter to 2 decimal places (all figures from here onwards shall we presented likewise) for each shape. These provide a measure of the overall difference in the scattering of the three shapes. We note that the hexagonal column and the column with stepped cavities have almost idenitical efficiencies and asymmetry parameter, whereas the efficiencies for the regular cavity column are lower, in particular the extinction efficiency. This is likely due to the angled cavity shape in this particle. This leads to a deflection of a greater portion of the incident wave's energy upwards, away from the scattering plane $\phi = 0$.

Shape	Q_{sca}	Q_{ext}	g	ω_0
Hex. col.	1.00	2.23	0.96	0.45
Reg. cav.	0.86	1.98	0.96	0.44
Step. cav.	0.97	2.18	0.96	0.44

Table 4: Scattering efficiencies and asymmetry parameter for the three scatterers at $ka = 10$ and $n = 1.0833 + 2.04e - 1i$.

Now let us consider the same problem at a weakly absorbing wavelength, namely at $\lambda = 0.55\mu m$ for which $n = 1.311 + 2.289e - 9i$. Figure 7 displays the same phase matrix elements as Figure 6 but at this second wavelength. We immediately see that the scattering patterns differ from each other more that for $\lambda = 10.87\mu m$. However, the elements can still be said to be similar until we exceed a scattering angle of 135°. Perhaps most notably, we observe that P_{22} (the departure of which from 1 is a measure of non-sphericity) for the stepped cavity appears markedly different. P_{22} for the stepped cavity fluctuates from 0 to 7% away from the constant lines of $P_{22} \approx 1$ for the other two columns.

The efficiencies in Table 5 suggest a greater difference in the scattering properties of these particles. We observe that Q_{sca} and Q_{ext} increase from the solid column to the regular cavity, and then further again to the stepped cavity, with this overall increase being almost 50%. However, ω_0 is much more similar for all three
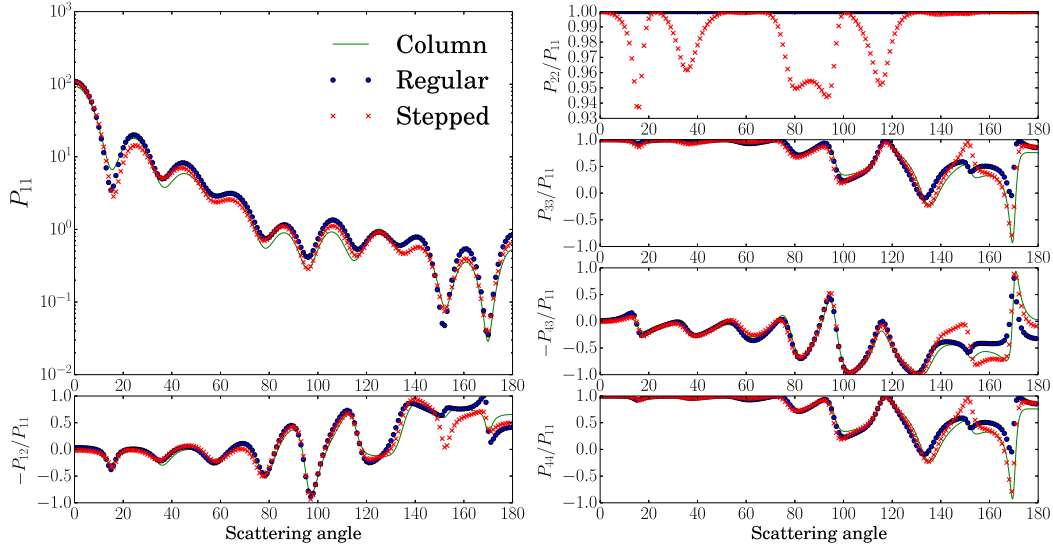
9

Figure 7: Scattering matrix elements for $n = 1.0833 + 2.04e - 1i$ and $ka = 10$ for the three scatterers in Figure 5.

shapes. g shows an increase of about 4% when going from the regular column to the stepped cavity (which is consistent with the increase in Q_{ext}).

Shape	Q_{sca}	Q_{ext}	g	ω_0
Hex. col.	2.05	2.06	0.79	0.99
Reg. cav.	2.62	2.64	0.80	0.99
Step. cav.	3.05	3.08	0.82	0.99

Table 5: Scattering efficiencies and asymmetry parameter for the three scatterers at $ka = 10$ and $\mu = 1.311 + 2.289e - 9i$.

8.2. Bullet-rosettes with 2 to 6 branches

Here we consider pristine bullet-rosettes. Each constituent branch of the bullet-rosettes is as in Figure 8, the dimensions of which are also illustrated in the figure. We take $L/(2R) = 2.5$ and $L/H = 3.09$ in accordance with the bullet-rosettes studied in [30]. The only difference between the bullet-rosettes here and those in [30] is that we introduce a small cube at the centre where the branches meet so that the scatterer's boundary is Lipschitz continuous. This requirement ensures that all the convergence theory for the BEM holds. The introduction of the cube makes a negligible difference to the scattering properties since it is chosen to be much smaller than the other dimensions of the shape, more precisely, the cube's side length is $(L + H)/50$.
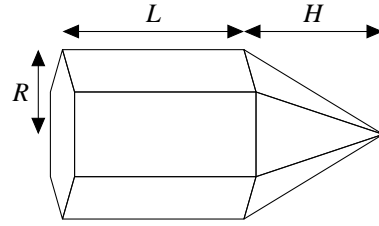

Figure 8: Illustration of a single constituent branch of the 2 to 6-branched bullet-rosettes.

The results presented here are for a refractive index of $n = 1.311 + 2.289e - 9i$ at a size parameter $kA = 15$ where $A := L + H$ is the radius of the smallest sphere which encloses the bullet-rosette. We shall use a mesh resolution of $\lambda/20$ in this section with the expectation of achieving 0.5% or better in the approximation accuracy for the scattering parameters, as indicated by the experiments in section 6.

Figure 9 shows the scattering matrix elements for bullet-rosettes with 3 to 6 branches. We have left out the 2 branch bullet as its scattering pattern is similar to the hexagonal column as presented in the previous section. For 4 branches onwards, a similar pattern in P_{11} begins to appear, with the peaks and troughs being located in approximately the same regions. The other matrix elements for these different bullet-rosettes are also similar, except for in the scattering region $80° < \vartheta < 130°$
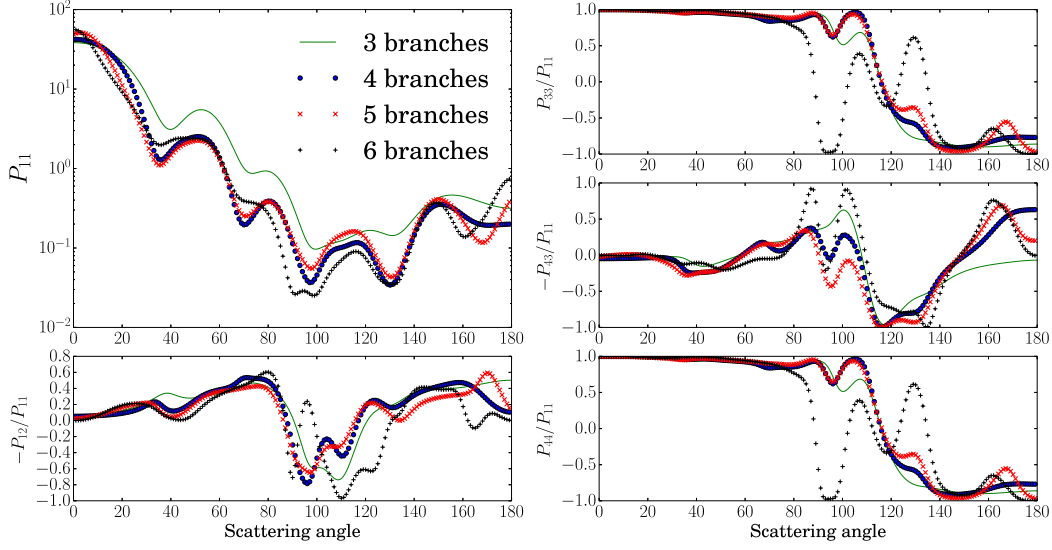
10

Figure 9: P_{11} for $n = 1.311 + 2.289e - 9i$ and $kA = 15$ for the bullet-rosettes with 3 to 6 branches.

where we see some strong differences. P_{22} has been omitted since, for all the bullet-rosettes here, it is approximately 1 for all scattering angles.

Table 6 shows the scattering efficiencies, asymmetry parameter and single-scattering albedo for the bullet-rosettes with 2 to 6 branches. We observe that the single-scattering albedo is very close to 1 for all shapes. We also note that the peak efficiencies appear for the 4-branched bullet-rosette. This is due to the increase of the projected cross section as we progress from 4 to 5 and 6 branches.

No. branches	Q_{sca}	Q_{ext}	g	ω_0
2	0.98	0.98	0.75	1.00
3	2.09	2.10	0.83	1.00
4	3.96	3.98	0.86	1.00
5	3.03	3.04	0.85	1.00
6	2.54	2.54	0.85	1.00

Table 6: Scattering efficiencies, asymmetry parameter and single-scattering albedo bullet-rosettes with 2 to 6 branches at $kA = 15$ and $n = 1.311 + 2.289e - 9i$.

9. Conclusion

The single scattering properties of ice particles in fixed orientation have been calculated using the re-

cently developed open source BEM library of Betcke et. al. [27]. In order to do this, we first established a system of boundary integral equations to be solved for this particular transmission problem. Currently BEM++ does not directly calculate the optical scattering properties of interest in atmospheric physics, so section 4 briefly explained how to obtain these properties from BEM++'s ouput.

Several examples of ice crystal shape were considered to confirm the validity and accuracy of the approximation produced by BEM++. Namely, spheres and hexagonal columns with differing refractive index and size parameter. For the sphere, the approximations produced by BEM++ were compared against those obtained using Mie-Lorenz theory. It was shown that BEM++ requires approximately 10 mesh elements per wavelength to attain approximately 1% accuracy in the scattering and extinction cross sections, however the accuracies in the phase function and asymmetry parameter are better than 1% at this resolution.

We further examined the performance of BEM++ by applying it to scattering by hexagonal ice columns and comparing the solution to that obtained with a highly accurate T-matrix method [3]. We found that, due to BEM++'s parallelisation, it runs considerably faster than the T-matrix method, however, its memory consumption is substantial. This large demand for memory limited the size parameter range to a maximum of ~15 on a quad core 16.4 Gigabyte machine, if an accuracy

11

of 1% is required. If a lower accuracy is required, or a larger machine is available, this size parameter range can of course be extended. Also, it should be noted that BEM++ is not exploiting the symmetries of the shape to reduce memory consumption as is done in [19, 24]. Hence, for non-symmetrical shapes, we can expect a similar size parameter range of application.

We demonstrated that, although the scattering and extinction efficiencies differed from those of the T-matrix by approximately 1%, the phase matrix entries were virtually indistinguishable. This allows us to be confident that the BIE formulation and meshing resolution we are using are sufficiently accurate for many applications of interest.

Finally, we showed examples where BEM++ can prove extremely useful, that is, in approximating the scattering by obstacles with more intricate shapes. We briefly explored the effect on the scattering of altering the shape of the cavities in hollow ice crystals. Further, we demonstrated that BEM++ may be used to investigate electromagnetic scattering by even more complicated ice crystal shapes, namely bullet-rosettes. It is worth mentioning that the scattering calculations for bullet-rosettes were fast and that higher size parameters can be achieved for such shapes as compared to spheres and hexagonal columns with aspect ratio 2 (as considered here) due to their smaller surface area.

We have not discussed scattering by particles in random orientation in this paper. This is one of the drawbacks of BEM compared to T-matrix. The T-matrix method allows analytic orientation averaging, whereas the current BEM approach requires the final system solve $x = A^{-1}b$ to be performed for numerous right-hand sides b, corresponding the incident field on the particle surface for different orientations, and then the solution averaged. This is seen in other methods such as the FDTD [3] and DDA, and proves to be slightly more costly than solving the same problem in fixed orientation in terms of CPU time. We emphasise that the process of calculating each b and solving the system is separate to the assembly of the matrix A which only needs to be performed once. The CPU times for the assembly of A are those presented in Table 2 and constitute the main computational load of the BEM. Calculating b and solving the system takes of the order of a few seconds for each orientation and so will not contribute significantly to the performance times if many solves are required. Also, performing these multiple solves will not increase the memory requirements, so the same size parameter range is available.

BEM++ is open source and available for download from the developers' website. This open availability along with the ability of boundary element methods to be applied to particles with arbitrary shapes are the main advantages of BEM++ over many other current methods. The Python scripts and meshes for the examples shown in this paper, and others, are available from the corresponding author.

10. Acknowledgements

[1] A. J. Baran. A review of the light scattering properties of cirrus. *J. Quant. Spectrosc. Ra.*, 110:1239–1260, 2009.

[2] A. J. Baran. From the single-scattering properties of ice crystals to climate prediction: A way forward. *Atmos. Res.*, 112:45–69, 2012.

[3] A. J. Baran, P. Yang, and S. Havemann. Calculation of the single-scattering properties of randomly oriented hexagonal ice columns: a comparison of the T-matrix and the finite-difference time-domain methods. *Appl. Optics*, 40(24):4376–4386, 2001.

[4] T. Betcke, S. Arridge, J. Phillips, M. Schweiger, and W. Śmigaj. Solution of electromagnetic problems using BEM++. In *Oberwolfach Report 03/2013*, pages 146–150, 2013.

[5] L. Bi, P. Yang, G. W. Kattawar, Y. Hu, and B. Baum. Scattering and absorption of light by ice particles: Solution by a new physical-geometric optics hybrid method. *J. Quant. Spectrosc. Ra.*, 112:1492–1508, 2011.

[6] L. Bi, P. Yang, G. W. Kattawar, and M. I. Mischenko. Efficient implementation of the invariant imbedding T-matrix method and the separation of variables method applied to large nonspherical inhomogeneous particles. *J. Quant. Spectrosc. Ra.*, 116:169–183, 2013.

[7] C. F. Bohren and D. R. Huffman. *Absorption and scattering of light by small particles*. John Wiley & Sons, Inc, 1983.

[8] A. Buffa and R. Hiptmair. Galerkin boundary element methods for electromagnetic scattering. In M. Ainsworth, editor, *Computational Methods in Wave Propagation*. Springer, New York, 2003.

[9] S. N. Chandler-Wilde, I. G. Graham, S. Langdon, and E. A. Spence. Numerical-asymptotics boundary integral methods in high-frequency acoustic scattering. *Acta Numer.*, pages 89–305, 2012.

[10] P. R. Field, J. Heymsfield, A. Bansemer, and C. H. Twohy. Determination of the combined ventilation factor and capacitance for ice crystal aggregates from airborne observations in a tropical anvil cloud. *J. Atmos. Sci.*, 65(2):376–391, 2008.

[11] S. P. Groth, D. P. Hewett, and S. Langdon. Hybrid numericalasymptotic approximation for high-frequency scattering by penetrable convex polygons. *IMA J. Appl. Math.*, 2013. doi: 10.1093/imamat/hxt040.

[12] S. Havemann and A. J. Baran. Extension of t-matrix to scattering of electromagnetic plane waves by non-axisymmetric dielectric particles: application to hexagonal ice cylinders. *J. Quant. Spectrosc. Ra.*, 70:139–158, 2001.

[13] L. Hesse, A. Macke, S. Havemann, A. J. Baran, Z. Ulanowski, and P. H. Kaye. Modelling diffraction by facetted particles. *J. Quant. Spectrosc. Ra.*, 113:342–347, 2012.

[14] Andrew J Heymsfield and Larry M Miloshevich. Relative humidity and temperature influences on cirrus formation and evolution: Observations from wave clouds and FIRE II. *J. Atmos. Sci.*, 52(23):4302–4326, 1995.

[15] M. Kahnert. The T-matrix code Tsym for homogeneous dielectric particles with finite symmetries. *J. Quant. Spectrosc. Ra.*, 123:62–78, 2013.

[16] R. P. Lawson, B. Pilson, B. Baker, Q. Mo, E. Jensen, L. Pfister, and P. Bui. Aircraft measurements of microphysical properties of subvisible cirrus in the tropical tropopause layer. *Atmos. Chem. Phys.*, 8:1609–1620, 2008. doi: 10.5194/acp-8-1609-2008.

[17] K. N. Liou. Influence of cirrus clouds on weather and climate processes: A global perspective. *Mon. Weather Rev.*, 114(6):1167–1199, 1986.

[18] A. Macke, J. Mueller, and E. Raschke. Single scattering properties of atmospheric ice crystals. *J. Atmos. Sci.*, 53(19):2813–2825, 1996.

[19] Y. Mano. Exact solution of electromagnetic scattering by a three-dimensional hexagonal ice column obtained with the boundary-element method. *Appl. Optics*, 39(30):5541–5546, 2000.

[20] P. A. Martin and P. Ola. Boundary integral equations for the scattering of electromagnetic waves by a homogeneous dielectric obtacle. *Proc. Roy. Soc. Edinburgh*, 123A:185–208, 1993.

[21] J. R. Mautz and R. F. Harrington. Electromagnetic scattering from a homogeneous material body of revolution. *Archiv Elektronik und Uebertragungstechnik*, 33:71–80, 1979.

[22] M. I. Mishchenko and L. D. Travis. Capabilities and limitations of a current FORTRAN implementation of the T-matrix method for randomly oriented, rotationally symmetric scatterers. *J. Quant. Spectrosc. Ra.*, 60(3):309–324, 1998.

[23] Karri Muinonen. Scattering of light by crystals: a modified kirchhoff approximation. *Appl. Optics*, 28(15):3044–3050, 1989.

[24] T. Y. Nakajima, T. Nakajima, Yoshimori K., S. K. Mishra, and S. N. Tripathi. Development of a light scattering solver applicable to particles of arbitrary shape on the basis of the surface-integral equations method of Müller type. I. methodology, accuracy of calculation, and electromagnetic current on the particle surface. *Appl. Optics*, 48(19):3526–3536, 2009.

[25] J. C. Nédélec. *Acoustic and Electromagnetic Equations: Integral Representations for Harmonic Problems*. Springer, New York, 2001.

[26] Kenneth Sassen, Zhien Wang, and Dong Liu. Global distribution of cirrus clouds from CloudSat/Cloud-Aerosol lidar and infrared pathfinder satellite observations (CALIPSO) measurements. *J. Geophys. Res.-Atmos.*, 113(D8), 2008.

[27] W. Śmigaj, T. Betcke, S. Arridge, J. Phillips, and M. Schweiger. Solving boundary integral problems with BEM++. *ACM T. Math. Software*, 2015. doi: 10.1145/2590830.

[28] H. R. Smith, A. Webb, P. Connolly, A. J. Baran, A. R. D. Smedley, and E. Hesse. Cloud chamber laboratory investigations into the scattering properties of hollow ice particles. *J. Quant. Spectrosc. Ra.*, 157:106–118.

[29] W. Sun, Q. Fu, and Z. Chen. Finite-difference time-domain solution of light scattering by dielectric particles with a perfectly matched layer absorbing boundary condition. *Appl. Optics*, 38(15):3141–3151, 1999.

[30] J. Um and G. M. McFarquhar. Single-scattering properties of aggregates of bullet rosettes in cirrus. *J. Appl. Meteor. Climatol.*, 46(6):757–775, 2007.

[31] S. G. Warren and R. E. Brandt. Optical constants of ice from the ultraviolet to the microwave: A revised compilation. *J. Geophys. Res.-Atmos.*, 113(D14), 2008.

[32] P. Yang and K. N. Liou. Geometric-optics-integral-equations method for light scattering by nonspherical ice crystals. *Appl. Optics*, 35(33):6568–6584, 1996.

[33] P. Yang, H. Wei, H.-L. Huang, B. A. Baum, Y. X. Hu, G. W. Kattawar, M. I. Mishchenko, and Q. Fu. Scattering and absorption property database for nonspherical ice particles in the near-through far-infrared spectral region. *Appl. Optics*, 44(26):5512–5523, 2005.

[34] E. Zubko, Y. Shkuratov, M. Mishchenko, and G. Videen. Light scattering in a finite multi-particle system. *J. Quant. Spectrosc. Ra.*, 109(12):2195–2206, 2008.